

Article

# The Role of Grain Size on Neutron Irradiation Response of Nanocrystalline Copper

Walid Mohamed <sup>1,\*†</sup>, Brandon Miller <sup>2</sup>, Douglas Porter <sup>2</sup> and Korukonda Murty <sup>1</sup>

<sup>1</sup> Department of Nuclear Engineering, North Carolina State University, Raleigh, NC 27695, USA; murty@ncsu.edu

<sup>2</sup> Idaho National Laboratory, P.O. Box 1625 Idaho Falls, ID 83415-6188, USA; brandon.miller@inl.gov (B.M.); douglas.porter@inl.gov (D.P.)

\* Correspondence: wmohamed@anl.gov; Tel.: +1-630-252-7418

† Current address: Nuclear Engineering Division, Argonne National Laboratory, Lemont, IL 60439, USA.

Academic Editor: Jie Lian

Received: 2 December 2015; Accepted: 23 February 2016; Published: 1 March 2016

**Abstract:** The role of grain size on the developed microstructure and mechanical properties of neutron irradiated nanocrystalline copper was investigated by comparing the radiation response of material to the conventional micrograined counterpart. Nanocrystalline (nc) and micrograined (MG) copper samples were subjected to a range of neutron exposure levels from 0.0034 to 2 dpa. At all damage levels, the response of MG-copper was governed by radiation hardening manifested by an increase in strength with accompanying ductility loss. Conversely, the response of nc-copper to neutron irradiation exhibited a dependence on the damage level. At low damage levels, grain growth was the primary response, with radiation hardening and embrittlement becoming the dominant responses with increasing damage levels. Annealing experiments revealed that grain growth in nc-copper is composed of both thermally-activated and irradiation-induced components. Tensile tests revealed minimal change in the source hardening component of the yield stress in MG-copper, while the source hardening component was found to decrease with increasing radiation exposure in nc-copper.

**Keywords:** copper; nanocrystalline; neutron irradiation; grain growth; radiation hardening; thermal stability

## 1. Introduction

The continuously increasing energy demand, combined with a noticeable depletion in traditional energy resources all over the world, has revived interest in developing advanced nuclear power systems—both fission and fusion based [1]. Proposed designs for the next generation of fission nuclear power reactors (Gen-IV) require both the fuel and structural materials to serve in more extreme operating conditions than current light water reactor designs. These conditions are imposed in order to satisfy stringent requirements such as longer life cycle, higher efficacy of energy conversion, and safety during normal and accidental conditions [2–4]. Similarly, the plasma-facing materials in fusion reactors will encounter a harsh radiation environment in order to achieve a higher level of durability and higher quality plasma [5,6]. Accordingly, the search for fuel and structural materials with high radiation resistance has become an inevitable challenge for the nuclear industry [7,8]. The well-known deterioration of mechanical, thermal and physical properties of materials in radiation environments at macroscopic scale is attributed to the accumulation of radiation induced point defects which leads to the formation of microscopic scale defect structures such as dislocations and voids [9]. Thus, the ability of a material to eliminate irradiation-induced point defects determines its radiation tolerance [10].

Nanocrystalline (nc) materials are polycrystals with a grain size <100 nm characterized by a large volume fraction of interfaces and triple junctions [11]. Because grain boundaries act as sinks for irradiation-induced point defects, it was hypothesized that nc materials would possess enhanced radiation resistance compared to conventional micrograined (MG) materials [12,13]. This is based on the premise that both the thermal stability and mechanical integrity of the nc materials will be maintained under irradiation [14]. The miniscule grain size of nc materials provides an excess of short diffusion paths for irradiation-induced point defects to migrate and annihilate at grain boundaries. Many studies have confirmed the enhanced radiation resistance of nc metals and alloys under a range of irradiation conditions in terms of radiation type, exposure level, and temperature. El-Atwani *et al.* [15] characterized the radiation response of nc and ultrafine grained tungsten in an *in-situ* 2 keV He ion irradiation conducted at 950 °C. A lower bubble density was observed in nc tungsten (grain size < 60 nm) compared to ultrafine-grained tungsten (grain size 100–500 nm). Kilmametov *et al.* [16] showed that a fully dense nc Ti-50.6at.%Ni alloy with a grain size of 23–31 nm had higher resistance to irradiation-induced amorphization compared to its MG counterpart following 1.5 MeV Ar<sup>+</sup> ion irradiation at room temperature. The influence of grain size on the density of defect clusters was investigated by Rose *et al.* [17], who observed a proportional decrease in defect density with decreasing grain size in nc ZrO<sub>2</sub> and Pd. Furthermore, researchers have also reported enhanced radiation resistance characteristics in various ultra-fine grained steel alloys following neutron and ion irradiations when compared to their MG counterparts [18–22].

In contrast, other studies in literature have shown evidence of thermal and structural instability of nc materials under irradiation. Kaoumi *et al.* [23] conducted an *in-situ* ion irradiation study on nc Zr, Pt, Cu, and Au to determine how the microstructure evolves under irradiation. Irradiation-induced grain growth was observed in all samples in the investigated temperature range of 20–773 K. Similarly, Nita *et al.* [24] reported an increase in grain size of Cu-0.5Al<sub>2</sub>O<sub>3</sub> from 178 to 493 nm, accompanied with formation of stacking faults and dislocations, after a 590 MeV proton irradiation to 0.91 dpa. Irradiation-induced grain growth in nc transition metals was also reported by Brogesen *et al.* [25], who irradiated thin films of nc Ni, Co, Cr, V, and Ti with 600 keV Xe ions at liquid nitrogen temperature to eliminate any potential occurrence of thermally-activated grain growth. Karpe *et al.* [26] characterized the developed microstructure of Ar<sup>+</sup> and Xe<sup>+</sup> irradiated Fe and Zr-Fe thin films with a grain size of 70–120 nm, and observed an increase in grain size at all exposure levels.

Thus, there is disagreement in the literature on the radiation resistance of nc metals and alloys, and the hypothesis of enhanced radiation resistance for this class of materials remains questionable to-date. Accordingly, a firm conclusion on the potential of nc materials as reactor materials necessitates further research to elucidate the behavior of these materials in radiation environments. Copper, the element of interest in this study, plays a major role in several nuclear applications due to its appealing thermal, mechanical, and physical properties. In the International Thermonuclear Experimental Reactor (ITER), the divertor components of the reactor are protected from the generated thermal energy of the plasma by the first wall which consists of a stainless steel shield bonded to a heat sink made of a copper-based alloy [27]. Additionally, the superconductor materials in fusion reactors are contained in a matrix of pure copper, which temporarily carries the electric current whenever the superconductors fail to do so [28]. Furthermore, copper is used in the fabrication of the canisters required for long term storage and isolation of spent nuclear fuel [29].

In this work, the influence of grain size on the response of nc-copper to fast neutron irradiation is investigated by exposing samples of nc-copper along with its MG counterparts to different damage levels. The scientific and technological importance of this work originates from the profound role of copper in nuclear applications as well as the obvious scarcity of neutron irradiation data in the literature of nc-copper in particular, and nc materials in general.

## 2. Experimental Details

### 2.1. Materials and Samples

The nc-copper investigated in this work was synthesized via the electrodeposition technique by the 3M Corporation, St. Paul, MN, USA, while the MG-copper samples were legacy materials from the Nuclear Material Laboratory at North Carolina State University. Energy dispersion spectroscopy (EDS) on a Hitachi S-3200 scanning electron microscope (SEM, Hitachi High Technologies in America, Clarksburg, WV, USA) was utilized to determine the copper purity of the MG and nc-copper samples, and they both were found to be 99.999%. In order to evaluate the microstructure and mechanical properties pre- and post-irradiation, sample of different geometries were prepared and irradiated: (i) 3 mm discs for microstructure characterization via transmission electron microscopy (TEM); (ii) 2 mm gauge length miniature tensile samples for tensile tests; and (iii) 3 mm × 5.3 mm plates for hardness measurements as well as non-destructive microstructure characterization techniques such as X-ray diffraction (XRD), atomic force microscopy (AFM), optical microscopy (OM), and SEM.

### 2.2. Irradiation Experiments

In this work, two irradiation facilities were utilized to expose the copper samples to a range of damage levels. The PULSTAR (This name refers to the ability of the reactor to produce short pulses of intense radiations) reactor in the Department of Nuclear Engineering at North Carolina State University was used for the low-dose irradiation and the Advanced Test Reactor (ATR) at Idaho National Laboratory (INL) for high dose exposures.

#### 2.2.1. Low Dose Irradiation at PULSTAR

PULSTAR is a 1MWth open pool reactor fueled with low enrichment  $\text{UO}_2$  in Zircaloy cladding with light water serving as a moderator and reflector. Samples of nc and MG-copper were sealed in evacuated quartz tubes and loaded in an aluminum canister (Figure 1a) inserted into a cadmium wrapped aluminum column in order to eliminate absorption of thermal neutrons by the samples. This minimizes the irradiation-induced activity via  $(n, \gamma)$  reactions, reducing the cooling time required for safe handling of the irradiated samples. Due to the inherent structure and other reactivity considerations of the PULSTAR core, the column containing the samples was not allowed to be irradiated near the core, where high neutron flux is achievable. Rather, the samples were irradiated in a vertical irradiation tube (West Rotating Exposure Port, WREP) at the core boundary (see Figure 1b), which limited the exposure level achievable in a reasonable time frame.

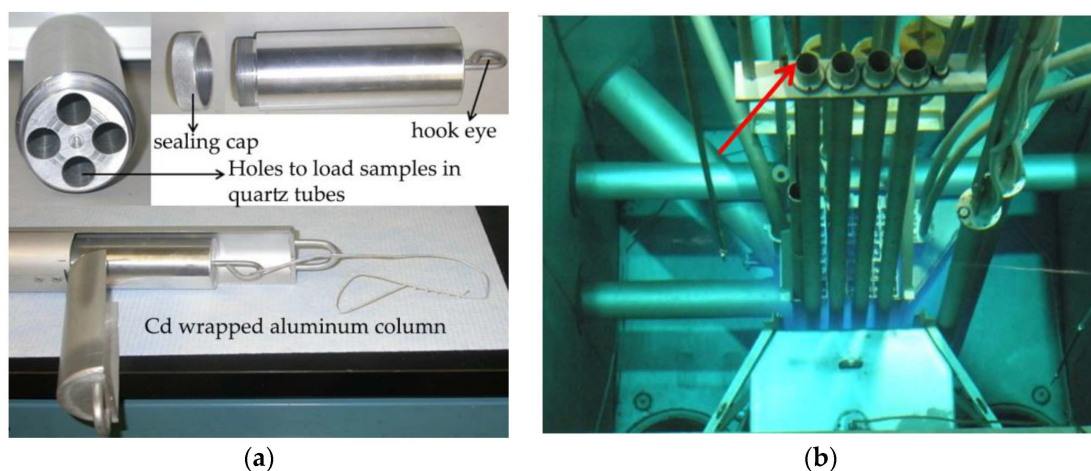


**Figure 1.** (a) Sample containment and Cd-wrapped aluminum column for neutron irradiation in PULSTAR; and (b) PULSTAR core with arrow indicating the WREP irradiation site.

High purity (99.999%) Ni foils were irradiated at the same vertical position as the aluminum canister and measurements of the induced activity in the foils were utilized to estimate the integrated fast neutron flux ( $E > 1.98 \text{ MeV}$ ) at the irradiation position; the flux is found to be  $\sim 2 \times 10^{12} \frac{n}{\text{cm}^2 \text{ sec}}$ . The copper samples were irradiated in the PULSTAR for 200 h at full power and the corresponding damage level in the samples was estimated to be  $\sim 3.4 \times 10^{-3} \text{ dpa}$ . Based on as-run experiments in PULSTAR, the maximum ambient temperature experienced by the copper samples during the irradiation was  $55 \text{ }^\circ\text{C}$ .

### 2.2.2. High Dose Irradiation at ATR

Two capsules holding samples of both nc and MG-copper were irradiated in the center position of the East Flux Trap (EFT) at position E-7 in the ATR core (Figure 2) [30]. Within each capsule, there was a test train assembly consisting of vertically stacked aluminum blocks designed to accommodate the different sample geometries. A thin aluminum disc was tack welded to the open end of each block to hold the samples, and the sample holder assemblies were strung together using thick aluminum wires, as depicted in Figure 3. Each test train was then sealed in a stainless steel capsule to prevent contact with the coolant water. The irradiation test assembly, as illustrated in Figure 2b, is comprised of the experiment basket, sleeve, and capsule assemblies. The assemblies contain the test trains (aluminum blocks and samples). The experiment basket of the test assembly is an aluminum tube that was designed to interface the capsule assembly with the EFT position E-7 in the ATR. The two capsules were irradiated concurrently for three ATR reactor cycles (144A, 144B, and 145A) to accumulate  $\sim 1 \text{ dpa}$  at damage rate of  $\sim 7.52 \times 10^{-7} \text{ dpa/s}$ . At the end of the first three cycles one capsule was withdrawn from the reactor core and the other capsule was irradiated for additional three cycles (145B, 146A, and 146B) to accumulate a total of  $\sim 2 \text{ dpa}$  of damage. The irradiation temperature of the copper samples in the capsules was calculated using the finite-element-based code Abaqus [31] in conjunction with Monte Carlo N-Particle (MCNP) code [32]. MCNP was utilized to provide the heat generation rate in each part of the capsule, which was then input into the Abaqus model. According to the calculated temperature distribution profiles shown in Figure 4, the irradiation temperature of the copper samples ranged from  $70 \text{ }^\circ\text{C}$  to less than  $100 \text{ }^\circ\text{C}$ .

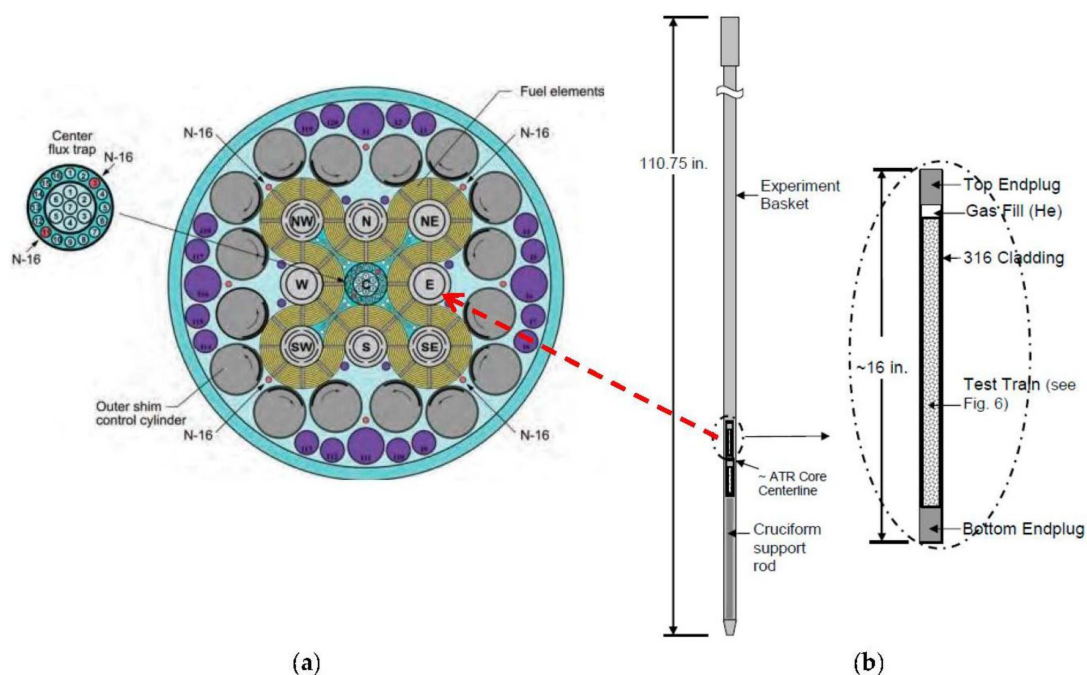


**Figure 2.** (a) Cross section view of ATR core with an arrow indicating irradiation test position E-7; (b) schematic of the irradiation test assembly for the ATR East Flux Trap Position.

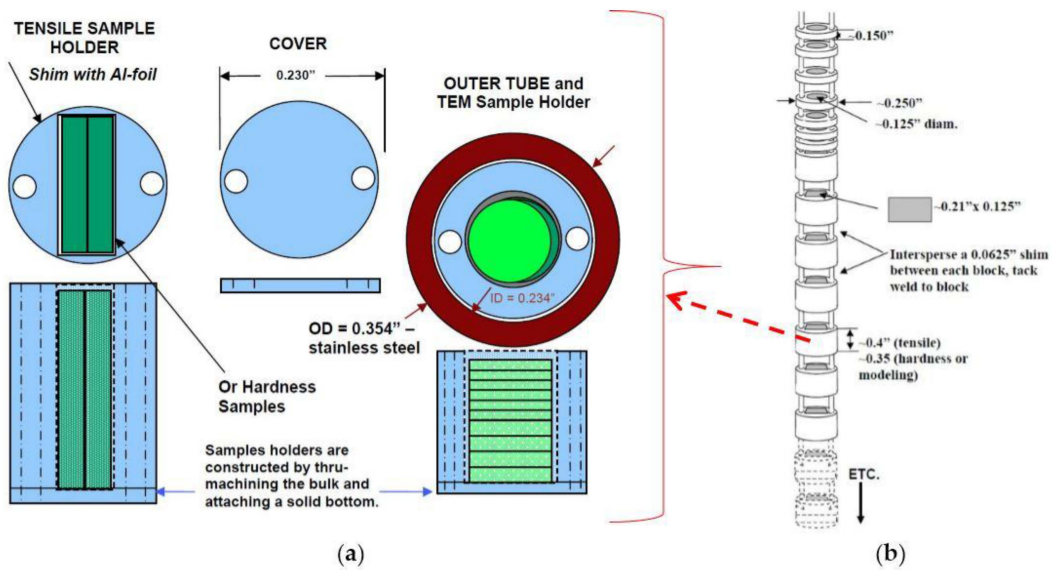


**Figure 3.** (a) Sample holder design for the ATR irradiation experiment; (b) schematic of the vertically stacked aluminum block sample holders in the test train assembly.

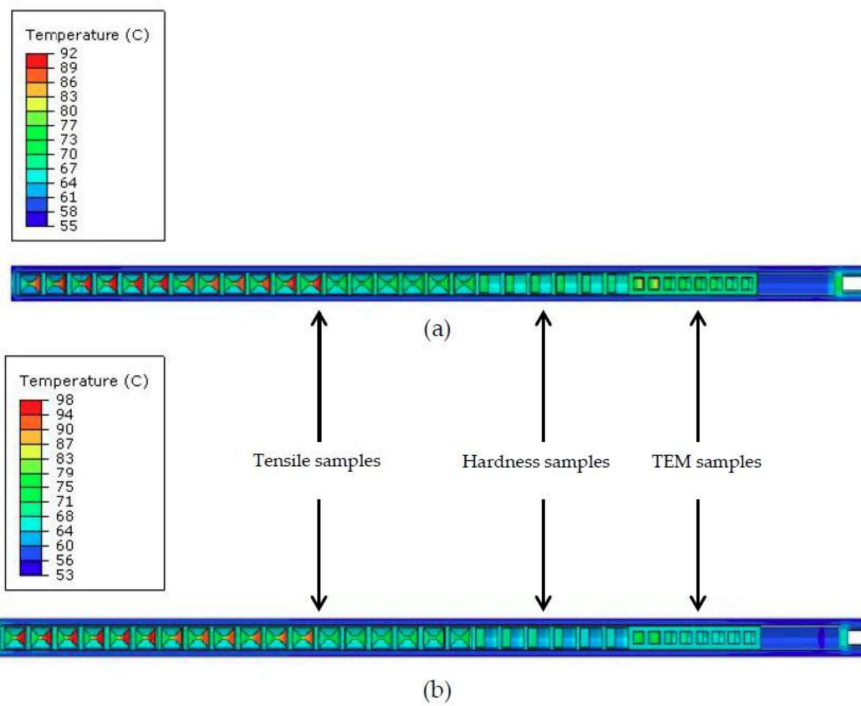


**Figure 4.** Irradiation temperature of copper samples as calculated by finite element model using Abaqus code in capsule irradiated up to (a) 1 dpa; and (b) 2 dpa.

### 2.3. Microstructure Characterization and Mechanical Testing

Several microstructural characterization techniques were utilized in order to investigate the microstructure of the copper samples pre- and post-irradiation. OM was utilized to determine the grain size distribution (GSD) and the average grain size of MG-copper using a chemical etchant consisting of 25% NH<sub>4</sub>OH + 25% H<sub>2</sub>O + 50% H<sub>2</sub>O<sub>2</sub>. The limited resolution power of OM prevented its applicability for characterization of the nc-copper samples. X-ray diffraction (XRD) patterns were recorded from MG- and nc-copper, pre- and post-irradiation, by a Rigaku smart lab diffractometer using CuK<sub>α</sub> radiation. The peak broadening observed in the nc-copper diffraction pattern enabled estimation of the

average grain size, using both the Scherrer formula [33,34] and the Williamson-Hall plot method [35]. Because XRD analysis provides only the average grain size, other characterization techniques were employed to establish the grain size distribution (GSD) of nc-copper. Atomic Force Microscopy (AFM) (Veeco-D3000, Veeco, Plainview, NY, USA) was utilized to determine both the average grain size and the grain size distribution of nc-copper. Its high resolution power allows counting of tens to hundreds of nano-grains over a scanning area of only a few micrometers. Microstructural characterization and analysis of defect structures were done using TEM. Typical 3 mm TEM discs were punched from both MG- and nc-copper, thinned down mechanically to a thickness of  $\sim 80 \mu\text{m}$ , and subjected to electrochemical thinning in an electrolyte solution of 10% nitric acid + 90% methanol maintained at  $-18 \text{ }^\circ\text{C}$  to create a thin electron transparent area on the foil. SEM was utilized to analyze the grain size of nc-copper.

Tensile testing and microhardness indentations were utilized to assess the influence of neutron irradiation on the mechanical properties of both MG- and nc-copper. All microhardness measurements reported in this work are based on a Vickers hardness setup using the Buehler OmniMet<sup>®</sup> microhardness testing system (Buehler, Lake Bluff, IL, USA). Although microhardness measurements directly reveal a material's hardness, it lacks information on other essential mechanical characteristics, such as ductility and toughness of the material, which can be determined through tensile testing. The limited availability of nc-copper material necessitated the utilization of sub-size tensile samples to assess the mechanical behavior. Although tensile samples of MG-copper could have been machined according to the American Society for Testing and Materials (ASTM) standard for tensile testing, it was decided instead to use sub-size tensile samples to avoid any potential effect related to sample geometry or dimensions when comparing to the nc-copper results. Tensile testing of the sub-size tensile samples was conducted with a miniature tensile tester (Figure 5a,b) that was built specifically for this purpose in the Nuclear Materials Laboratory at North Carolina State University (Typical tensile grips were used for tensile testing of irradiated samples at INL using Instron 5967 dual column testing system (Instron, Grove City, OH, USA). All tensile tests were conducted at room temperature at a constant strain rate of  $10^{-5} \text{ s}^{-1}$ .

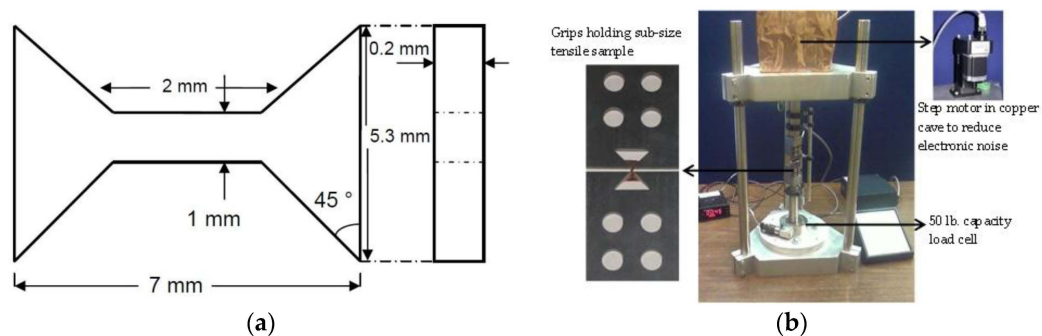


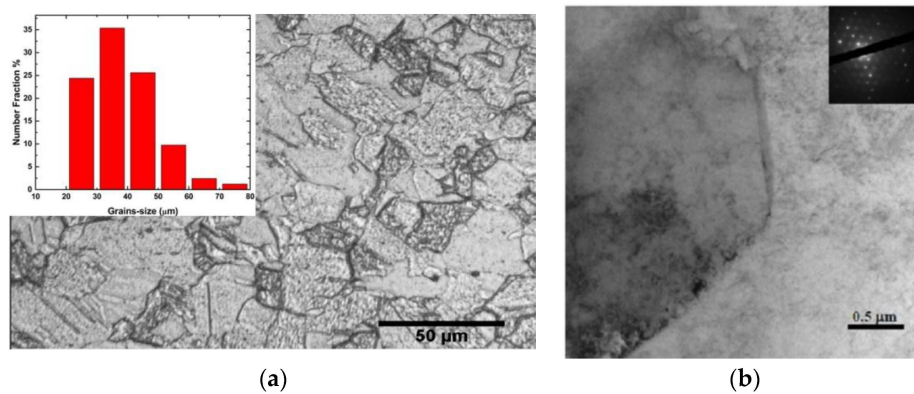
**Figure 5.** (a) Schematic of sub-size tensile sample; (b) photograph of the miniature tensile tester for mechanical loading of sub-size tensile samples.

### 3. Results and Discussion

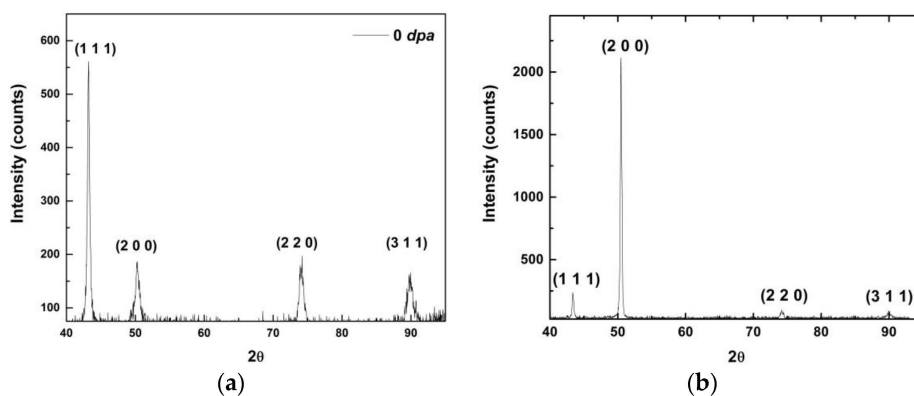
#### 3.1. Microstructure and Mechanical Properties of As-Received Materials

Figure 6a is an optical micrograph of as-received MG-copper used to determine the GSD of the material. The average grain size of MG-copper was found to be  $\sim 38 \pm 12 \mu\text{m}$ . Figure 6b shows TEM microstructure of the as-received MG-copper depicting no major defects. The average grain size of nc-copper was determined through several methods, including XRD, AFM, and TEM image analyses. Figure 7 depicts the XRD patterns of nc- and MG-copper, where major reflection peaks are identified. The difference in peak broadening between nc- and MG-copper is primarily due to crystallite size-induced broadening. Due to the grain size difference between nc- and MG-copper,

there is substantial broadening induced in nc-copper, but grain size has almost no effect in the diffraction pattern of MG-copper. Analyses of the XRD pattern of nc-copper based on both the Scherrer formula and the Williamson-Hall plot method indicated average grain sizes of 17 and 44 nm, respectively. The GSD of the as-received nc-copper was established from an AFM micrograph taken over a  $1 \mu\text{m} \times 1 \mu\text{m}$  scanning area (Figure 8a, b). It can be seen that the grain size of nc-copper varied between 10 and 100 nm, and the corresponding average grain size of the material was found to be  $\sim 48 \pm 16$  nm.



**Figure 6.** (a) Optical micrograph of as-received MG-copper with corresponding GSD inset showing average grain size  $\sim 38 \pm 12 \mu\text{m}$ ; and (b) Bright field TEM of as received MG-copper, with the corresponding diffraction pattern inset.



**Figure 7.** XRD patterns with major reflection peaks identified for (a) nc-copper; and (b) MG-copper.

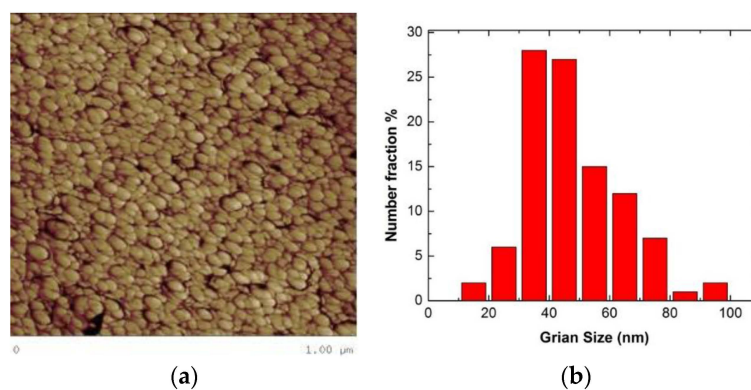


**Figure 8.** (a) AFM micrograph of as-received nc-copper; and (b) corresponding GSD showing variation in grain size between 10 and 100 nm with average grain size  $\sim 48 \pm 16$  nm.

The bright field TEM image of the as-received nc-copper, along with the corresponding diffraction pattern, is shown in Figure 9a where the near-to-complete diffraction rings are characteristic of a nanocrystalline material with randomly-oriented grains. Due to the large number of grains in each specific crystallographic plane, nc-copper forms rings rather than individual diffraction spots as observed in MG-copper. The GSD distribution of nc-copper based on TEM characterization is shown in Figure 9b and the corresponding average grain size of the material was found to be  $\sim 28 \pm 11$  nm. Finally, the average grain size of as-received nc-copper was defined to be  $\sim 34.4$  nm from averaging all the values obtained by XRD, AFM, and TEM techniques.

Hardness measurements were made over an  $8 \text{ mm} \times 6 \text{ mm}$  area of the as-received materials to ensure homogeneity of the microstructure. The average microhardness of MG- and nc-copper was found to be  $\sim 0.6 \pm 0.02$  GPa and  $2.5 \pm 0.05$  GPa, respectively. Further evaluation of the mechanical properties of the as-received materials was achieved through tensile testing of sub-size tensile samples of MG and nc-copper. The resultant engineering stress-strain curves shown in Figure 10 were utilized to determine the engineering yield stress ( $S_y$ ), the ultimate tensile strength (UTS), uniform strain ( $e_u$ ), total engineering strain ( $e_t$ ), and the strain hardening exponent ( $n$ ) of both materials as listed in Table 1.

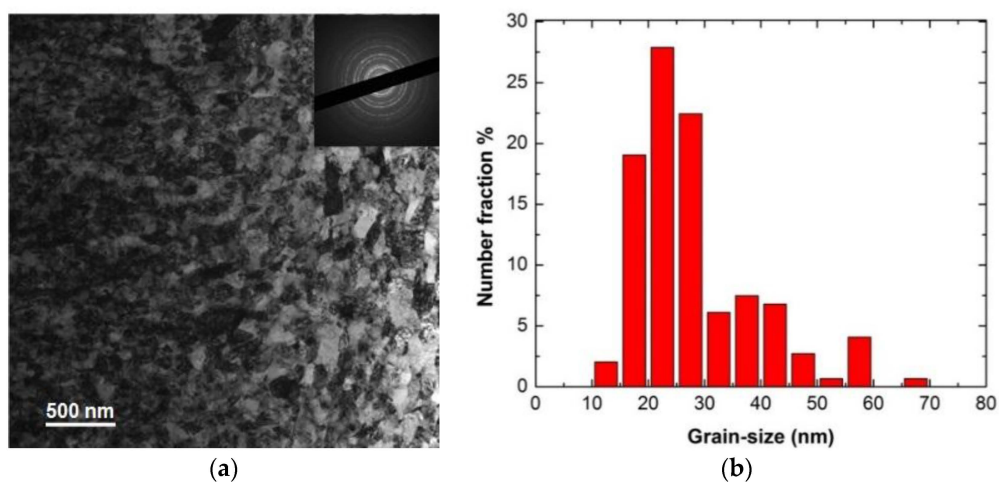


**Figure 9.** (a) Bright field TEM of as-received nc-copper; and (b) corresponding GSD with average grain size  $\sim 28 \pm 11$  nm.

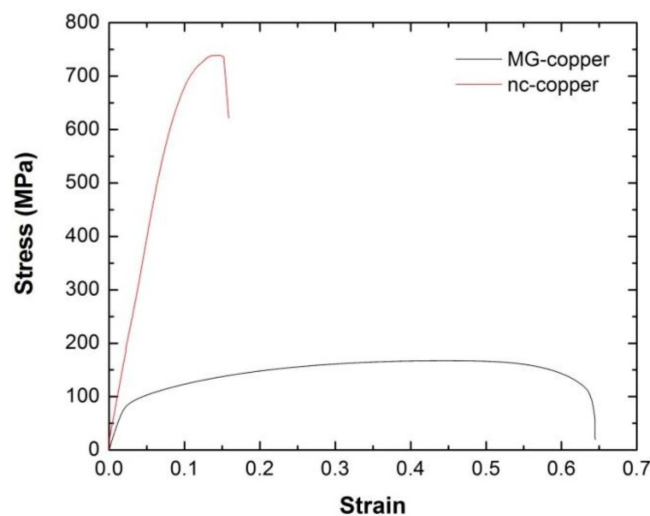


**Figure 10.** Engineering stress-strain curves of as-received MG and nc-copper from tensile testing at room temperature and strain rate of  $10^{-5} \cdot \text{s}^{-1}$ .

**Table 1.** Mechanical properties of MG and nc-copper pre- and post-irradiation (0 dpa refers to data of as-received material).

Exposure Level	S <sub>y</sub> (MPa)	UTS (MPa)	e <sub>u</sub>	e <sub>t</sub>	n
<b>MG-copper</b>					
0 dpa	80 ± 6	174 ± 21	0.43 ± 0.07	0.66 ± 0.02	0.35 ± 0.05
0.0034 dpa	187 ± 7	215 ± 8	0.21 ± 0.06	0.34 ± 0.05	0.19 ± 0.05
1 dpa	260 ± 16	265 ± 9	0.089 ± 0.04	0.22 ± 0.02	0.085 ± 0.04
2 dpa	323 ± 40	323 ± 40	0.065 ± 0.00	0.21 ± 0.02	0.063 ± 0.00
<b>nc-copper</b>					
0 dpa	557 ± 5	731 ± 21	0.052 ± 0.004	0.079 ± 0.001	0.05 ± 0.004
0.0034 dpa	371 ± 15	372 ± 15	0.05 ± 0.001	0.18 ± 0.014	0.00
1 dpa	357 ± 8	358 ± 9	0.005 ± 0.001	0.029 ± 0.007	0.00
2 dpa	388 ± 20	389 ± 30	0.007 ± 0.004	0.036 ± 0.005	0.00

From the data in Table 1, MG-copper possesses much higher ductility and toughness (from the uniform and total strain values) compared to nc-copper. From yield and UTS values, nc-copper has a higher overall strength compared to MG-copper as expected from grain refinement. The difference in strength and ductility between nc-copper and its micrograined counterpart is germane to the difference in grain size reported in the preceding subsection. The material's strength evolves with an increasing density of pinning points, such as grain boundaries, which are capable of hampering the mobility and propagation of imperfections (dislocations). Thus, it is plausible to ascribe the observed high strength and poor ductility of nc-copper to the increased grain boundary density upon grain refinement, and the ability of those grain boundaries to act as pinning points. This effect is commonly referred to as the Hall-Petch grain boundary strengthening mechanism [36] accordingly:

$$\sigma_y = \sigma_i + \frac{K_y}{\sqrt{d}} \quad (1)$$

where  $\sigma_y$  is the yield stress;  $\sigma_i$  is the friction stress;  $K_y$  is strengthening coefficient (a material constant); and  $d$  is the grain size. According to Equation (1), the yield stress of a material increases with decreasing the average grain size which explains the observed high yield stress of nc-copper (grain size ~34 nm) compared to that of its MG counterpart (grain size ~38  $\mu$ m).

### 3.2. Mechanical Properties and Microstructure of Irradiated MG-Copper

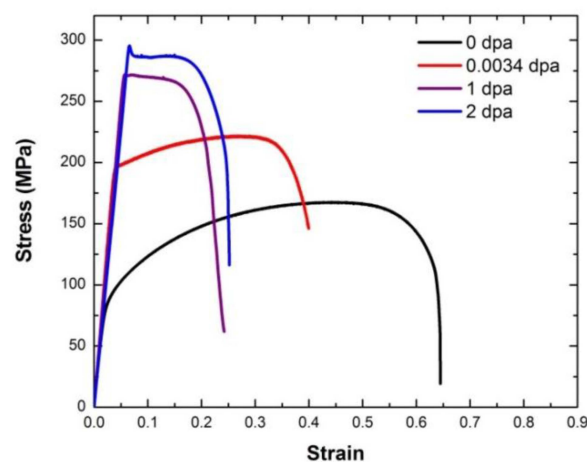
Microhardness measurements and tensile testing of irradiated MG-copper were conducted following the same procedures as for the as-received material. Microhardness measurements of irradiated MG-copper, listed in Table 2, reveal a steep increase in hardness due to 0.0034 dpa of damage. This sudden change in hardness is followed by a saturation, which may start below or at about 1 dpa. Saturation in hardness of neutron irradiated oxygen-free high-purity copper was observed by Singh *et al.* [37] to occur between 0.1 and 0.2 dpa, consistent with the behavior observed in this study.

**Table 2.** Microhardness measurements (GPa) of MG- and nc-copper post irradiation.

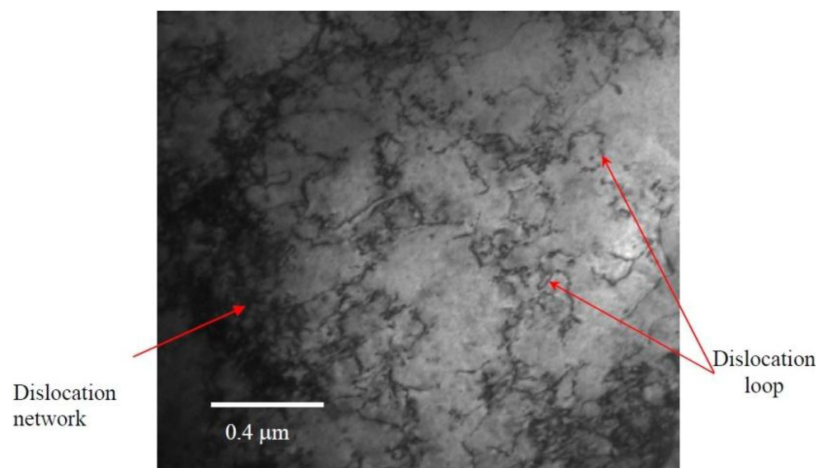
Material	0 dpa	0.0034 dpa	1 dpa	2 dpa
MG-copper	0.60 ± 0.02	0.75 ± 0.02	1.07 ± 0.01	1.08 ± 0.02
nc-copper	2.51 ± 0.05	1.91 ± 0.11	1.15 ± 0.03	1.16 ± 0.04

Figure 11 shows the engineering stress-strain curves of MG-copper, and the average mechanical properties of the material are listed in Table 1 from which the evolution of the mechanical behavior of MG-copper with damage level can be summarized by an increase in strength (both yield and ultimate) accompanied by a loss in ductility (both uniform and total elongation), jointly referred to as irradiation

hardening and embrittlement. Close scrutiny of the mechanical properties of irradiated MG-copper indicates a more profound increase in yield stress compared to the UTS. Moreover, the difference between yield and ultimate strength was found to diminish with increasing damage level implying decreased work hardening ( $n$ ) with increased neutron dose. Of interest is the yield drop phenomenon clearly observed in MG-copper at 2 dpa (Figure 11). Using OM, the average grain size of irradiated MG-copper was found to be  $39 \pm 7$ ,  $37 \pm 11$ , and  $49 \pm 14$   $\mu\text{m}$  after 0.0034, 1, and 2 dpa, respectively. Thus, it is possible to state that no grain growth occurred in irradiated MG-copper. This is consistent with the fact that thermally-induced grain growth occurs in MG-copper only at relatively elevated temperatures ( $> 600$   $^{\circ}\text{C}$ ) [38] while the maximum irradiation temperature experienced by MG-copper samples was less than  $100$   $^{\circ}\text{C}$  (Figure 4). Characterization of the irradiation-induced defect structures in MG-copper using TEM revealed dislocation loops and networks in the grain interior at 0.0034 dpa (Figure 12).



**Figure 11.** Engineering stress-strain curves of irradiated MG-copper.



**Figure 12.** Bright field TEM micrograph of MG-copper at 0.0034 dpa showing dislocation loops and networks in the grain interior.

As the damage level increased to 1 dpa, dislocation loops and networks were observed in both the grain interior (Figure 13a) as well as at grain boundaries (Figure 13b). Inspection of the TEM micrographs (Figures 12 and 13) indicates a higher dislocation density in the more heavily damaged sample. A twin structure was also observed (Figure 13c), a feature that became more common with increasing damage level. At 2 dpa, TEM characterization of MG-copper revealed formation of relatively

higher dislocation density (Figure 14a) along with abundant twin structures in grains with curved boundaries as depicted by the dotted curve in Figure 14b.

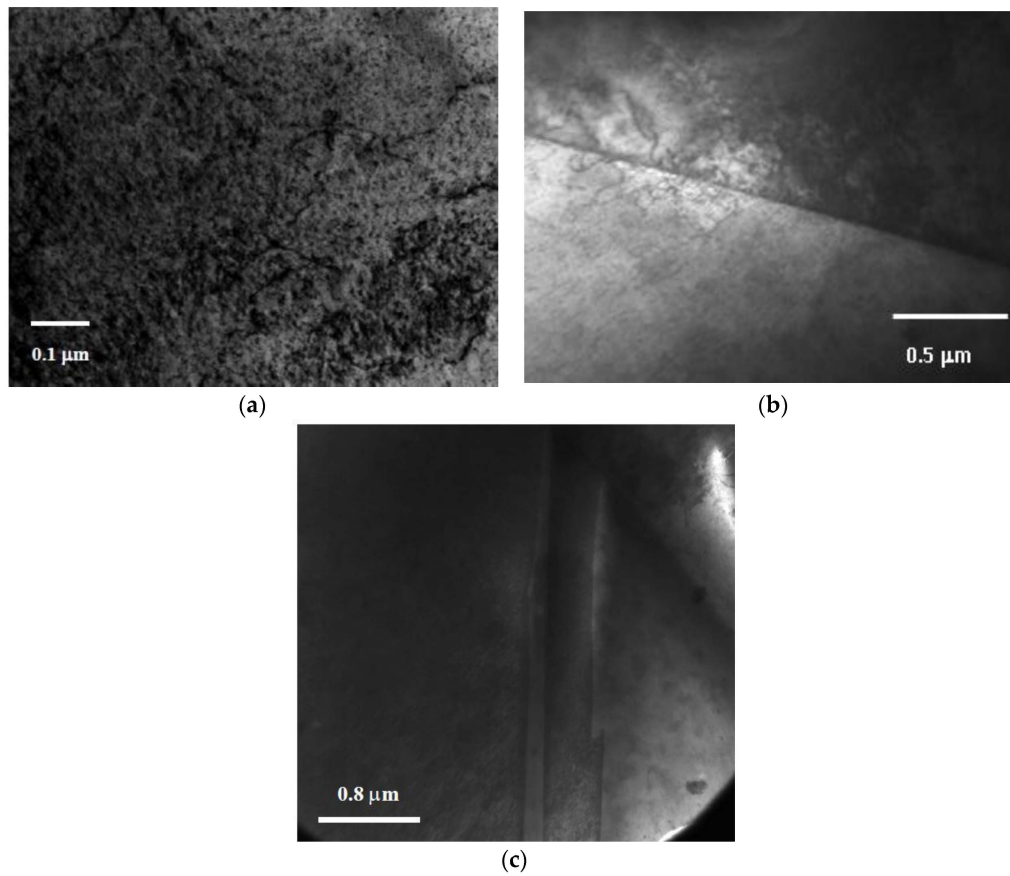


**Figure 13.** Bright field TEM micrographs of MG-copper at 1 dpa showing (a) dislocations in the grain interior; (b) dislocations at the grain boundary; and (c) twin structure.

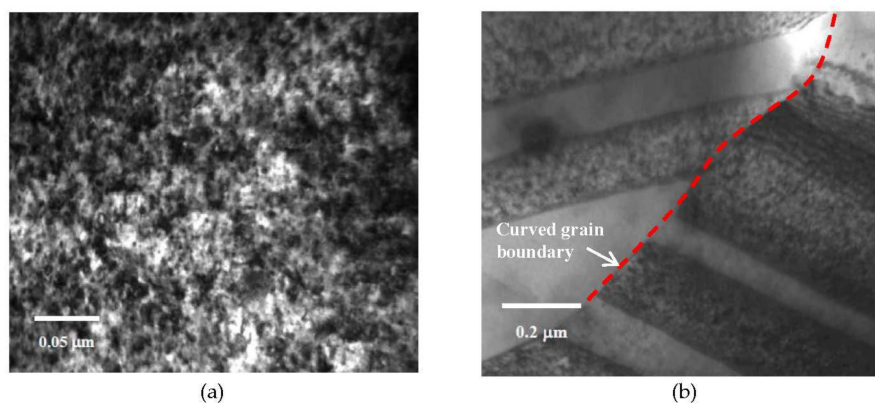


**Figure 14.** Bright field TEM images of MG-copper at 2 dpa showing formation of (a) high dislocation density; and (b) twin structures in a grain with curved boundary.

At this point, the relationship between yield strength and the developed microstructure in irradiated MG-copper can be elaborated by considering the yield stress in irradiated material as [39]:

$$\sigma_y = \sigma_i + \sigma_s \quad (2)$$

where  $\sigma_i$  is the friction hardening; and  $\sigma_s$  is the source hardening. Source hardening is commonly found in irradiated FCC metals (e.g., copper) where radiation-induced defects are present close to Frank-Read (F-R) sources. This increases the stress required for F-R operation and consequently contributes not only to increasing the yield stress but also yield point phenomena of irradiated materials. Friction hardening is the stress experienced by the mobile dislocations encountering irradiation-induced obstacles such as precipitates, voids, or other dislocations during their glide/slip. In the context of radiation hardening, the friction hardening component is usually decomposed into two components as follows:

$$\sigma_i = \sigma_{SR} + \sigma_{LR} \quad (3)$$

where  $\sigma_{SR}$  is short range friction hardening; and  $\sigma_{LR}$  is long range friction hardening [39]. The classification here depends on the type of obstacles responsible for inhibiting dislocation motion.  $\sigma_{SR}$  arises from dislocation pinning by irradiation-induced defects such as voids and precipitates. As no voids or precipitates were observed in irradiated MG-copper,  $\sigma_{SR}$  can be set to zero in Equation (3).  $\sigma_{LR}$  arises from the repulsive force experienced by a mobile dislocation due to long range stress fields of forest dislocations. The contribution of long range friction hardening to the yield stress of irradiated material is given by [40]:

$$\sigma_{LR} = \alpha G b \sqrt{\rho_d} \quad (4)$$

where  $\alpha$  is a constant,  $G$  is the shear modulus,  $b$  is the Burgers vector, and  $\rho_d$  is the dislocation density. Equation (4) indicates that the long range component of friction hardening, and consequently the overall yield stress, is proportional to the dislocation density in the irradiated material. Thus, it is plausible to ascribe the continuous increase in yield stress of irradiated MG-copper with exposure level to the observed increase in radiation induced defects (dislocations in particular). An approach to decompose the yield stress in irradiated MG-copper into source hardening and friction hardening components will be discussed in Section 3.4 of this article.

### 3.3. Mechanical Properties and Microstructure of Irradiated nc-Copper

#### 3.3.1. Mechanical Properties of Irradiated nc-Copper

Microhardness indentation and tensile testing were conducted on nc-copper after irradiation following the same procedures applied to MG-copper. According to the microhardness measurements listed in Table 2, irradiated nc-copper exhibits a steep decrease in hardness following 0.0034 dpa irradiation. The decrease in hardness seems to saturate either below or at 1 dpa. After that, only a minor increase in hardness was observed between 1 and 2 dpa. This is in contrast to irradiated MG-copper where hardness was found to increase at all damage levels achieved in this study. Representative engineering stress-strain curves of irradiated nc-copper are shown in Figure 15 and the average mechanical properties of irradiated nc-copper based on the analysis of stress-strain curves of two samples are included in Table 1. We note that nc-copper exhibited a substantial decrease in yield stress and UTS, accompanied by an increase in total elongation, following 0.0034 dpa irradiation. This decrease in both yield stress and UTS post irradiation is referred to as irradiation-induced softening [41,42]. Yield stress and UTS further decreased after 1 dpa irradiation, although less dramatically. This was accompanied by a substantial decrease in both uniform and total elongation to below even its pre-irradiation values. Finally, nc-copper exhibited typical radiation hardening and embrittlement at 2 dpa, manifested by an increase in both yield stress and UTS accompanied by a loss of ductility. Thus, based on the analyses of hardness measurements and mechanical properties of irradiated nc-copper the following two observations are made: (i) radiation softening was noted in the material up to 1 dpa; and (ii) nc-copper exhibited common radiation hardening at 2 dpa. This differed from the radiation response of MG-copper, where radiation hardening was observed at all damage levels.

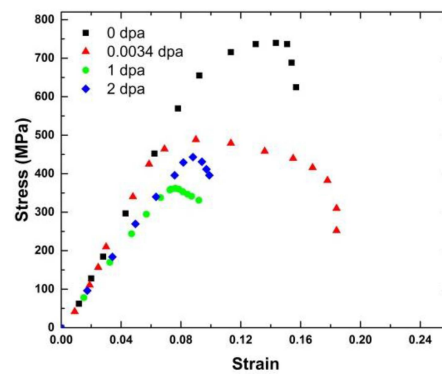


**Figure 15.** Representative engineering stress-strain curves of irradiated nc-copper.

### 3.3.2. Microstructural Characterization of Irradiated nc-Copper

Figure 16 shows XRD patterns of irradiated nc-copper compared to the as-received material. The observed decrease in peak broadening (in terms of FWHM) at 0.0034 dpa implies an increase in the grain size at this damage level; the average grain size of nc-copper at 0.0034 was found to be  $\sim 70$  nm. The reduction in peak broadening continued through 1 and 2 dpa, where peak broadening was below the limit to determine the average grain size with XRD. The variation in peak intensity in XRD patterns from one damage level to another indicates a change in the relative grain population in a particular crystallographic direction. Thus, the 0.0034 dpa irradiation resulted in a rearrangement of grain orientation such that the peak of highest intensity changed from (111) to (200). For both 1 and 2 dpa samples, the (111) peak exhibited the highest intensity, similar to the case of as-received material. Finally, the presence of only the four major diffraction peaks of copper at all damage levels indicates no second phase formation in the irradiated material. Figure 17 shows an AFM image of nc-copper following 0.0034 dpa and the average grain size of the material was found to increase from  $48 \pm 16$  to  $65 \pm 10$  nm after irradiation. Therefore, the results from both XRD analysis and AFM suggest that nc-copper underwent grain growth during 0.0034 dpa irradiation.

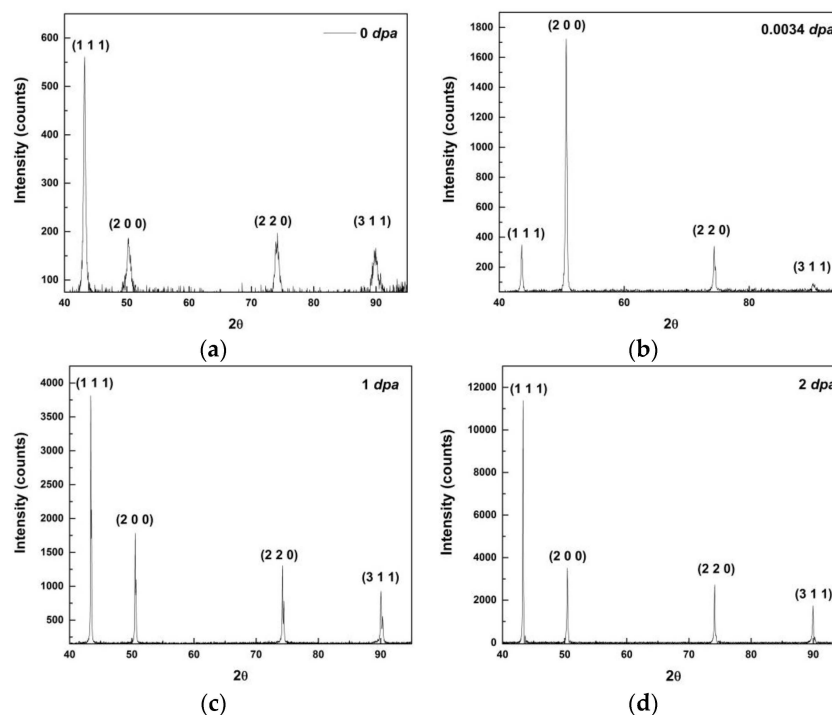


**Figure 16.** XRD patterns of nc-copper (a) as-received; (b) at 0.0034 dpa; (c) at 1 dpa; and (d) at 2 dpa.

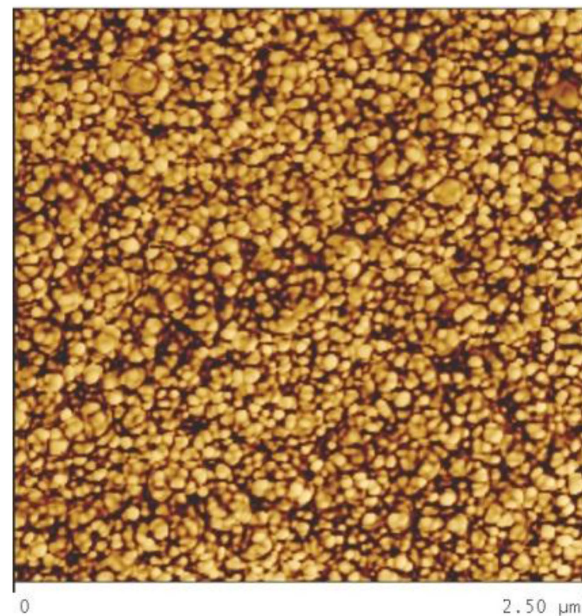


**Figure 17.** AFM image of nc-copper post 0.0034 irradiation with an average grain size of  $65 \pm 10$  nm.

TEM characterization revealed several microstructural features in nc-copper at 0.0034 dpa. Figure 18a shows the presence of twins and dislocation structures in the irradiated material. These defect structures were not observed in the as-received material, implying that some grains have grown enough to accommodate these defects. However, this sample still contains nanosized grains, as observed in other regions, as indicated by near to complete diffraction rings in Figure 18b. The GSD of nc-copper at this damage level was established by combining the distributions from both AFM and TEM characterization (Figure 19) and the corresponding average grain size was found to be  $86 \pm 38$  nm. The relatively wide range of grain size observed in the material suggests the occurrence of non-uniform grain growth at this exposure level. Formation of twin and dislocation structures are noted in nc-copper irradiated to 1 dpa (Figure 20a). In addition, nc-copper with this damage level exhibited formation of twin structures at faceted grain boundaries as depicted by dashed lines in Figure 20b. At 2 dpa, twin and dislocation structures were the most pronounced microstructural features (Figure 21). Interestingly, we note twin structures at curved grain boundaries, similar to that observed in MG-copper at the same damage level (depicted by the dotted curve in Figure 21b).

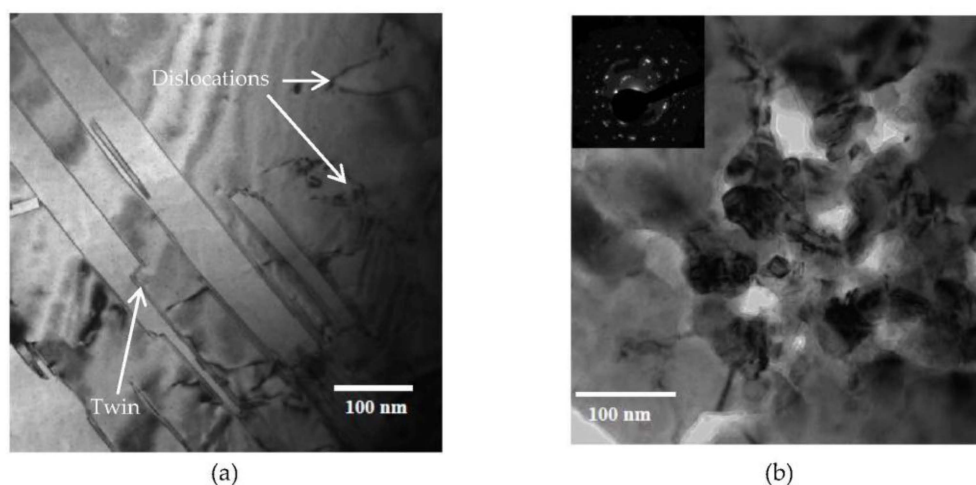


**Figure 18.** Bright field TEM of nc-copper at 0.0034 dpa showing (a) formation of both complete and incomplete twin and dislocation structures; and (b) population of grains with diameter  $< 100$  nm.

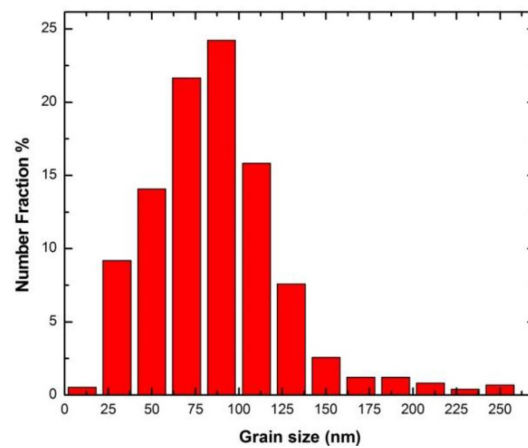


**Figure 19.** Grain size distribution (GSD) of irradiated nc-copper at 0.0034 dpa showing average grain size  $\sim 86 \pm 38$  nm.

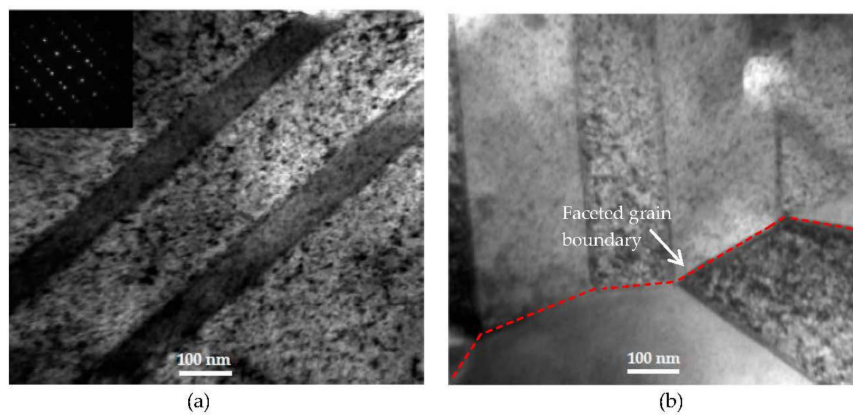


**Figure 20.** Bright field TEM of nc-copper at 1 dpa showing (a) formation of twin and dislocation structures; and (b) twin structures formed at a faceted grain boundary.

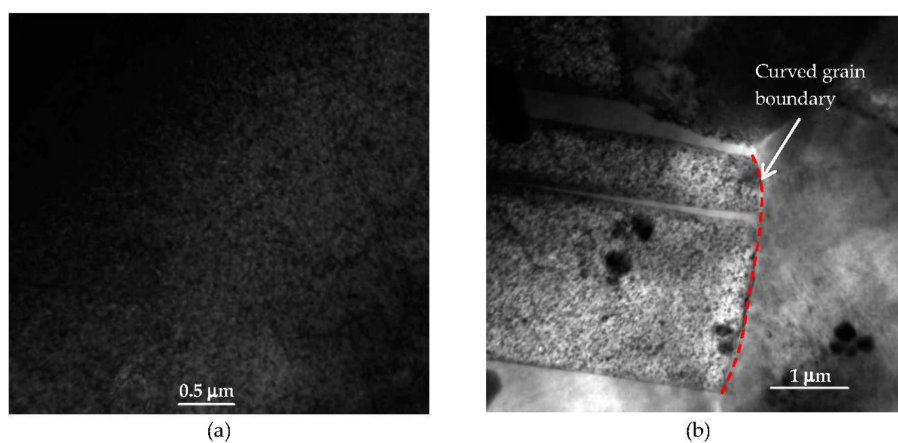


**Figure 21.** Bright field TEM of nc-copper at 2 dpa showing (a) formation of dislocation structures; and (b) twin structures formed at a curved grain boundary.

It is worthwhile to mention that nanograins were not observed in any TEM foil from nc-copper after either the 1 or 2 dpa irradiations. However, attempts to determine grain size of nc-copper at 1 and 2 dpa using OM were not successful, as the grain sizes were still too small to be resolved with this technique. Thus, the average grain size and GSD of irradiated nc-copper at 1 and 2 dpa were

determined using SEM (Figure 22) to be  $\sim 0.8 \pm 0.6 \mu\text{m}$  and  $0.75 \pm 0.5 \mu\text{m}$  at 1 and 2 dpa, respectively. Thus, irradiated nc-copper exhibited an increase in the average grain size with exposure levels starting at 0.0034 dpa. After that, saturation in grain growth occurred at around 1 dpa, as depicted by the dotted lines in Figure 23.

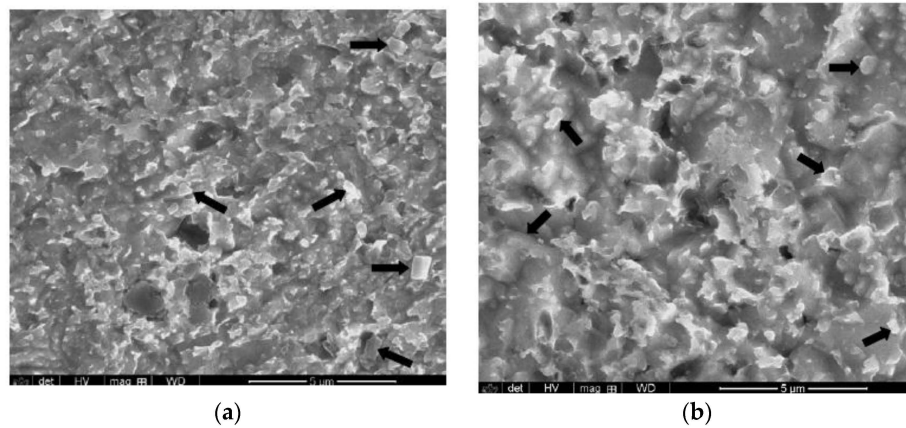


**Figure 22.** SEM images of irradiated nc-copper at (a) 1 dpa; and (b) 2 dpa with arrows pointing at typical grains considered for grain size measurements.

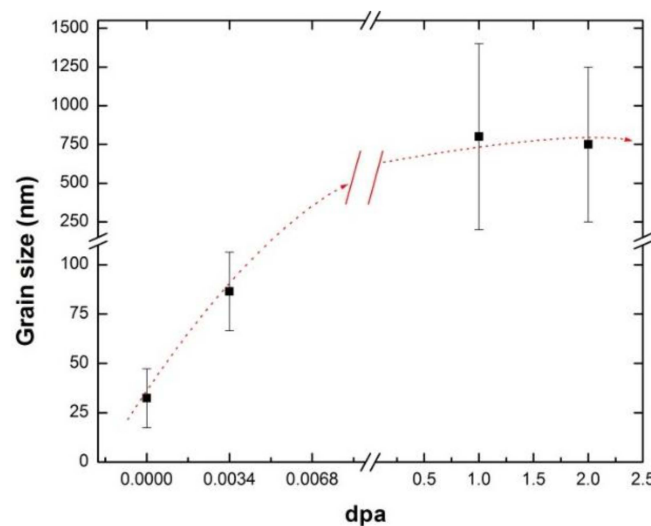


**Figure 23.** Variation of the average grain size of irradiated nc-copper with exposure level, showing grain growth at 0.0034 dpa and minimal change in average grain size between 1 and 2 dpa.

At this point, it is possible to elaborate the structure-property relationship in irradiated nc-copper by considering the Hall-Petch relationship (Equation (1)) and the friction and source hardening components comprising the yield stress (Equation (2)):

$$\sigma_y = \sigma_i + \sigma_s = \sigma_i + \frac{K_y}{\sqrt{d}} \quad (5)$$

The substantial decrease in the yield stress of nc-copper from  $\sim 557$  to  $371$  MPa at 0.0034 dpa is attributed to the increase in grain size from  $\sim 34$  to  $86$  nm. As grain growth persisted, the average grain size increased to the submicron level ( $\sim 800$  nm) at 1 dpa, resulting in a further decrease in the yield stress. At this damage level, grains in irradiated nc-copper have grown enough to accommodate complex forms of defects, such as dislocations and twins. At higher doses the yield stress decreased moderately from  $\sim 371$  to  $357$  MPa, accompanied by loss of ductility reflecting the

grain size saturation. Accordingly, it is plausible to state that the mechanical behavior of nc-copper at high doses was not solely controlled by grain growth. After 1 dpa, no further grain growth was observed in irradiated nc-copper, so the mechanical behavior of the material was governed by common radiation hardening and embrittlement. This was manifested by an increase in yield stress from ~357 to 388 MPa, accompanied by ductility loss.

### 3.3.3. Grain Growth in Irradiated nc-Copper

The overall mechanical behavior and microstructural evolution in irradiated nc-copper reveals that grain growth has a detrimental effect on the overall radiation response of the material, even at very low exposure levels. This necessitates investigating how grain growth in nc-copper originated under the irradiation conditions in this study. Thermally-activated grain growth has been observed in nc metals and alloys well below the temperature required to trigger grain growth in its MG counterparts [43]. Thereby, a series of annealing experiments followed by hardness and grain size measurements were conducted on as-received nc-copper to assess its thermal stability. Samples of as-received nc-copper were isothermally annealed in vacuum for three hours at temperature ranges from ~300 to 750 K. Subsequently, grain size measurements were conducted and the average grain size was determined. Figure 24 plots the average grain size *versus* annealing temperature with the box in Figure 24a expanded in Figure 24b.

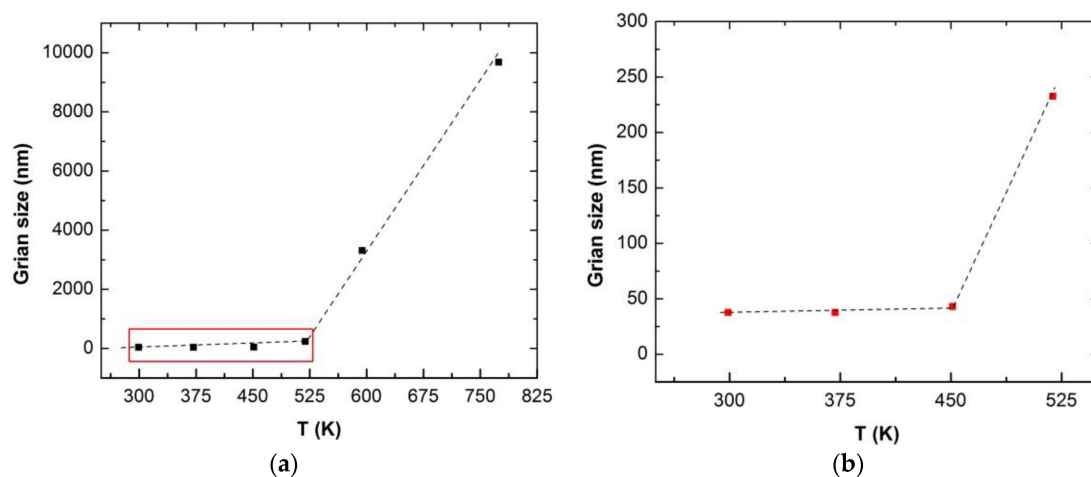


**Figure 24.** Variation of grain size of nc-copper with annealing temperature showing (a) sudden change in grain growth rate at ~520 K; and (b) onset of thermal instability at ~450 K.

The variation of grain size with annealing temperature reveals a sudden increase in the grain growth rate at ~520 K. The change in grain growth rate implies that thermally-activated grain growth in nc-copper is controlled by two distinct mechanisms. Kinetics of isothermal grain growth is typically described by the following rate equation:

$$D^n \approx K_0 \exp\left(\frac{-Q}{RT}\right) t \quad (6)$$

where  $D$  is the grain size at time  $t$ ;  $K_0$  is a pre-exponential constant;  $n$  is the grain growth exponent;  $Q$  is the activation energy for a specific grain growth mechanism;  $R$  is the gas constant; and  $T$  is the annealing temperature. Thus, the activation energy for thermally-activated grain growth in as-received nc-copper was determined by plotting grain size *versus* inverse temperature for several grain growth exponent ( $n$ ) values (see Figure 25). With  $n$  set to 5, the activation energy for grain growth of as-received nc-copper at temperatures above ~520 K was found to be ~55 kcal/mole. This is in reasonable agreement with the 46.8 kcal/mole reported for the activation energy of lattice diffusion in MG-copper [44]. At temperatures below 520 K, the activation energy of nc-copper was found to be

$\sim 22$  k kcal/mole for  $n = 5$ . This is in agreement with the activation energy for grain boundary diffusion reported in some nc metals and alloys [45].

In addition to isothermal annealing experiments, Differential Scanning Calorimetry (DSC) was used to determine the temperature at which thermally activated grain growth is triggered in nc-copper. Details about the theory behind this technique can be found elsewhere [46]. DSC Q2000 series from TA Instruments (Wood Dale, IL, USA) was used to anneal a 3 mm disk of the as-received nc-copper at a rate of 10 K/min and Figure 26 shows the heat flow through the sample as a function of measured sample temperature. According to the DSC scan, the onset of thermal instability in as-received nc-copper occurs at approximately 450 K ( $\sim 170$  °C) and the full peak is observed at 520 K ( $\sim 235$  °C) (Figure 26). Recalling the isothermal annealing data of as-received nc-copper, grain growth via grain boundary diffusion was dominant at  $\sim 450$  K which coincides with the onset of thermal instability observed with the DSC scan. Furthermore, the transition from grain boundary diffusion to lattice diffusion at  $\sim 520$  K (247 °C) is in good agreement with the formation of the full peak thermal instability at  $\sim 235$  °C in the DSC scan. Thus, it is concluded that temperature regime in which thermally-activated grain growth is controlled by grain boundary diffusion represents the onset to thermal instability in nc-copper. Thus, the observed grain growth in irradiated nc-copper can be separated into thermal and irradiation effects. Additional isothermal annealing experiments were conducted on samples of nc-copper at 328 K (55 °C) for 200 hrs and at 373 K (100 °C) for up to 740 hrs. This mimics the highest irradiation temperature and time in the PULSTAR and ATR, respectively.

The hardness of the annealed samples with annealing time at the two temperatures is included in Figure 27a,b. The as-received nc-copper annealed at 55 °C for 200 hrs exhibited a noticeable reduction in hardness. This implies an increase in grain size in light of the Hall-Petch equation. However, thermally-activated grain growth induced by annealing cannot be the sole cause of the observed decrease in hardness of nc-copper after the 0.0034 dpa irradiation. Thus, it is possible to split the grain growth in irradiated nc-copper at 0.0034 dpa into two components: (i) thermally-activated component (indicated by dotted arrows in Figure 27a); and (ii) irradiation-induced component (indicated by solid arrows in Figure 27a). Clearly, the irradiation-induced component of grain growth is more dominant at this damage level. Figure 27b indicates that grain growth in nc-copper irradiated to 1 and 2 dpa can be attributed to both a thermally-activated component and an irradiation-induced component, as in the 0.0034 dpa case. Both components contribute approximately equally to the overall grain growth at these exposure levels.

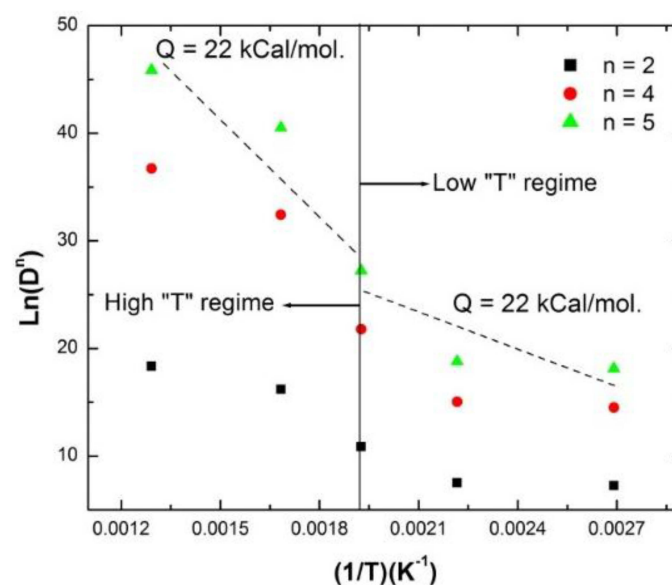


**Figure 25.** Arrhenius plot analyzing thermally-activated grain growth in as-received nc-copper.

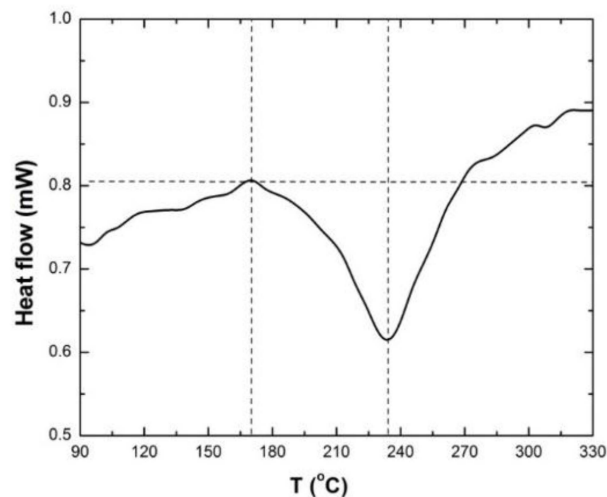


Figure 26. DSC scan of 3 mm disk of as-received nc-copper at heating rate of 10 K/min.

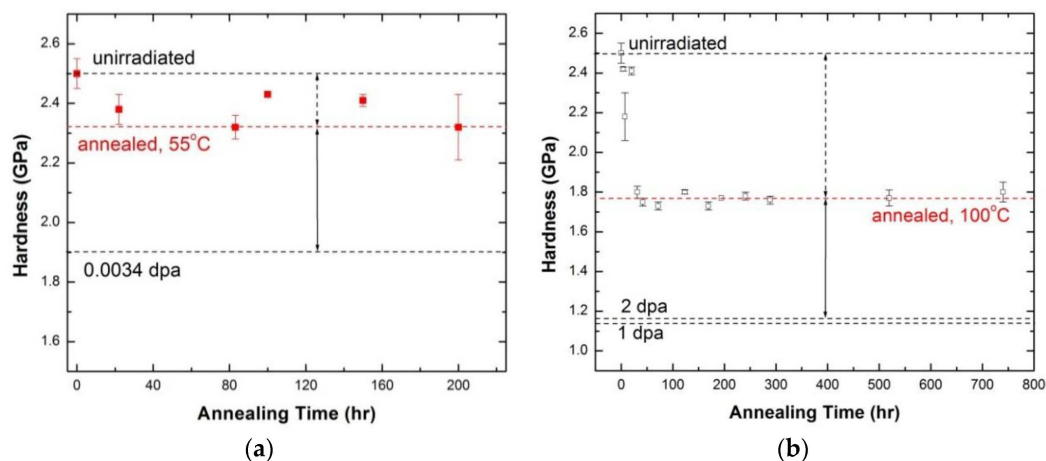
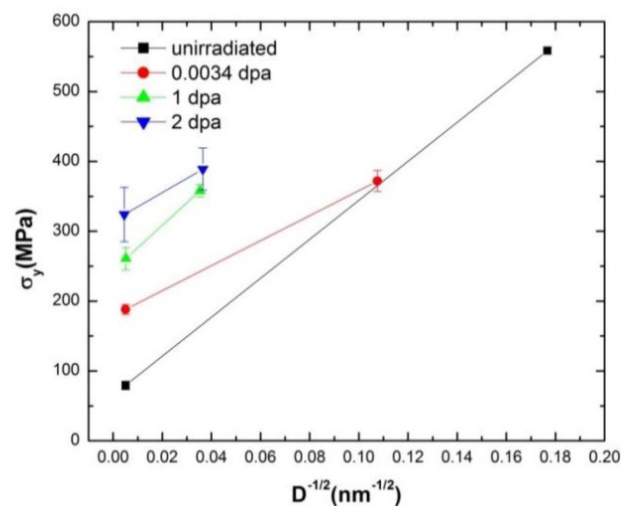


Figure 27. Variation of hardness of nc-copper with annealing time at (a) 55 °C; and (b) 100 °C, with dashed lines indicating the hardness of the material under the marked conditions.

While the mechanisms controlling thermally-induced grain growth in nc-copper were able to be identified, determination of the underlying mechanism for irradiation-induced grain growth in in-pile experiments is not possible due to limited data. Studies investigating the mechanisms of radiation-induced grain growth are primarily based on computational and simulation efforts [47]; however, there is no well-defined explanation of the mechanisms for this process to-date. Alternatively, the researchers are considering *in-situ* ion irradiation experiments combined with real-time TEM to understand the driving force and mechanisms underlying radiation-induced grain growth in nc-copper.

### 3.4. Radiation Hardening in Polycrystalline Copper

Radiation hardening was observed in both MG-copper and nc-copper. In MG-copper, radiation hardening was observed at all damage levels while it became dominant in nc-copper only at higher damage levels. In this section, radiation hardening in irradiated MG and nc-copper will be decomposed into source and friction components in light of Equation (5). The variation in yield stress of irradiated MG and nc-copper with grain size is plotted at each damage level in Figure 28. This allows investigating the influence of grain size and exposure level simultaneously on the mechanical behavior of polycrystalline materials.



**Figure 28.** Variation of yield stress with grain size at all exposure level.

From Figure 28, the variation in the yield stress of irradiated polycrystalline copper can be thought to follow a general Hall-Petch behavior, albeit only two data points (representing MG and nc-copper) are present. A close scrutiny of the data reveals that the slope of Hall-Petch line inconsistently changes from one exposure level to the other. Friction and source components were examined by fitting the two data points at each damage level to a straight line. The slope of that straight line corresponds to the unpinning stress  $K_y$  and the source hardening can then be calculated as  $\frac{K_y}{\sqrt{d}}$  for both MG and nc-copper. Consequently, the friction hardening is calculated as the difference between yield and source hardening stresses. This approach relies on the premise that the straight lines are representative of the effect of radiation exposure on the yield stress and the unpinning stress,  $K_y$ . The variation in friction hardening of polycrystalline copper is shown in Figure 29a. Clearly, irradiated polycrystalline copper exhibited an increase in friction hardening with increasing exposure level, as depicted by the dashed curve (Figure 29a). This is attributed to the observed increase in dislocation density in both MG and nc-copper with increasing exposure level. The source hardening component of the yield stress *versus* damage level is shown in Figure 29b and nc-copper exhibits a continuous decrease in source hardening with damage level. This is ascribed to the observed increase in grain size from 34.4 nm pre-irradiation to about 1  $\mu\text{m}$  after irradiation to 1 and 2 dpa. Conversely, the source hardening of irradiated MG-copper does not vary significantly with damage, implying that source hardening has only a minimal contribution to the yielding of irradiated MG-copper.

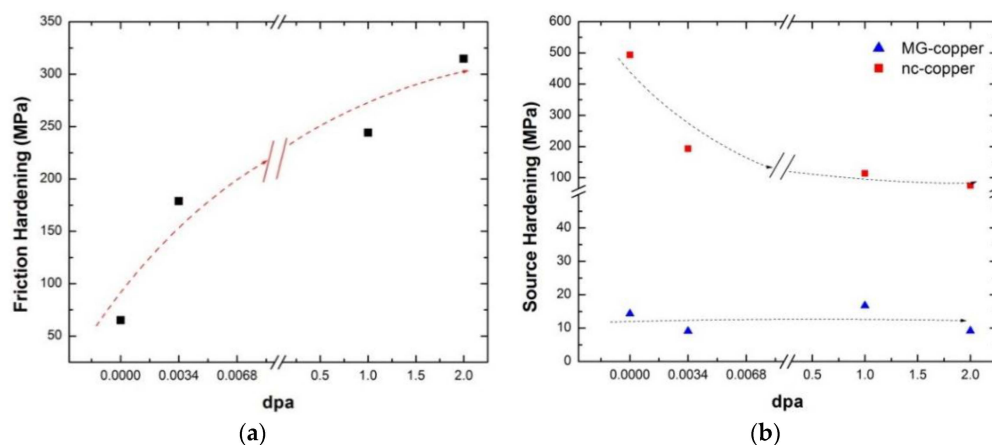


**Figure 29.** Variation of (a) friction hardening; and (b) source hardening of polycrystalline copper with exposure level.

#### 4. Summary and Conclusions

The impact of grain size on the response of MG and nc-copper to fast neutron irradiation was assessed by evaluating the mechanical behavior and microstructural evolution in the material pre and post-irradiation. The following remarks were drawn:

- MG-copper exhibited typical radiation hardening and embrittlement at all damage levels achieved in this work.
- At low exposure levels, nc-copper experienced grain growth, and radiation softening was noted by a dramatic decrease in strength accompanied by increased ductility.
- The increase in grain size of irradiated nc-copper allowed formation of complex defect forms, such as twins and dislocations, at higher damage levels.
- Radiation hardening became dominant in irradiated nc-copper after grain growth saturation at higher exposure levels.
- Analysis of isothermal annealing and hardness measurements revealed that grain growth in nc-copper is composed of both thermally-activated and irradiation-induced components.
- The yield stress data of irradiated MG and nc-copper were analyzed on the basis of the Hall-Petch relationship.
- Friction hardening was found to increase with an increasing damage level in polycrystalline copper.
- Source hardening in irradiated nc-copper was found to decrease with an increasing damage level, while it has minimal contribution to the yield stress of irradiated MG-copper.

**Acknowledgments:** This work is supported by the NSUF-ATR through the US Department of Energy (DOE), Office of Nuclear Energy under DOE Idaho Operations Office Contract DE-AC07-051D14517. The authors wish to thank Joseph W. Nielsen for reactor environment and material damage calculations and Paul E. Murray for the thermal (Abaqus) calculations.

**Author Contributions:** Walid Mohamed performed experiments, samples characterization, mechanical testing, data analysis, and wrote this manuscript. Brandon Miller performed materials characterization, data analysis and supported experiments at INL. Douglas Porter managed experiments and supported data analysis at INL. Korukonda Murty supervised experiments at North Carolina State University, supported data analysis, and reviewed this manuscript.

**Conflicts of Interest:** The authors declare no conflict of interest.

#### References

1. Neklyudov, I.M.; Voyevodin, V.N. Radiation swelling of modified austenitic steels. *Russ. Phys. J.* **2008**, *51*, 400–413. [[CrossRef](#)]
2. Yvon, P.; Carré, F. Structural materials challenges for advanced reactor systems. *J. Nucl. Mater.* **2009**, *385*, 217–222. [[CrossRef](#)]
3. Murty, K.L.; Charit, I. Structural materials for Gen-IV nuclear reactors: Challenges and opportunities. *J. Nucl. Mater.* **2008**, *383*, 189–195. [[CrossRef](#)]
4. Abram, T.; Ion, S. Generation-IV nuclear power: A review of the state of the science. *Energy Policy* **2008**, *36*, 4323–4330. [[CrossRef](#)]
5. Duffy, D.M. Fusion power: A challenge for materials science. *Philos. Trans. A Math. Phys. Eng. Sci.* **2010**, *368*, 3315–3328. [[CrossRef](#)] [[PubMed](#)]
6. Zinkle, S.J.; Victoria, M.; Abe, K. Scientific and engineering advances from fusion materials R & D. *J. Nucl. Mater.* **2008**, *311*, 31–42.
7. Mansur, L.; Rowcliffe, A.; Nanstad, R.; Zinkle, S.; Corwin, W.; Stoller, R. Materials needs for fusion, Generation IV fission reactors and spallation neutron sources—Similarities and differences. *J. Nucl. Mater.* **2004**, *329–333*, 166–172. [[CrossRef](#)]
8. Zinkle, S.J.; Was, G.S. Materials challenges in nuclear energy. *Acta Mater.* **2013**, *61*, 735–758. [[CrossRef](#)]
9. Singh, B.N.; Foreman, A.J.E.; Trinkaus, H. Radiation hardening revisited: Role of intracascade clustering. *J. Nucl. Mater.* **1997**, *249*, 103–115. [[CrossRef](#)]

10. Misra, A.; Demkowicz, M.J.; Zhang, X.; Hoagland, R.G. The radiation damage tolerance of ultra-high strength nanolayered composites. *J. Miner.* **2007**, *59*, 62–65. [[CrossRef](#)]
11. Suryanarayana, C. Nanocrystalline materials. *Int. Mater. Rev.* **1995**, *40*, 41–64. [[CrossRef](#)]
12. Chang, Y.-Q.; Guo, Q.; Zhang, J.; Chen, L.; Long, Y.; Wan, F.-R. Irradiation effects on nanocrystalline materials. *Front. Mater. Sci.* **2013**, *7*, 143–155. [[CrossRef](#)]
13. Zhang, X.; Fu, E.G.; Li, N.; Misra, A.; Wang, Y.-Q.; Shao, L.; Wang, H. Design of radiation tolerant nanostructured metallic multilayers. *J. Eng. Mater. Technol.* **2012**, *134*. [[CrossRef](#)]
14. Wurster, S.; Pippin, R. Nanostructured metals under irradiation. *Scr. Mater.* **2009**, *60*, 1083–1087. [[CrossRef](#)]
15. El-Atwani, O.; Hinks, J.A.; Greaves, G.; Gonderman, S.; Qiu, T.; Efe, M.; Allain, J.P. *In-situ* TEM observation of the response of ultrafine- and nanocrystalline-grained tungsten to extreme irradiation environments. *Sci. Rep.* **2014**, *4*. [[CrossRef](#)] [[PubMed](#)]
16. Kilmametov, A.R.; Gunderov, D.V.; Valiev, R.Z.; Balogh, A.G.; Hahn, H. Enhanced ion irradiation resistance of bulk nanocrystalline TiNi alloy. *Scr. Mater.* **2008**, *59*, 1027–1030. [[CrossRef](#)]
17. Rose, M.; Balogh, A.G.; Hahn, H. Instability of irradiation induced defects in nanostructured materials. *Nucl. Instrum. Methods Phys. Res. Sect. B* **1997**, *128*, 119–122. [[CrossRef](#)]
18. Alsabbagh, A.; Sarkar, A.; Miller, B.; Burns, J.; Squires, L.; Porter, D.; Cole, J.I.; Murty, K.L. Microstructure and mechanical behavior of neutron irradiated ultrafine grained ferritic steel. *Mater. Sci. Eng. A* **2014**, *615*, 128–138. [[CrossRef](#)]
19. Alsabbagh, A.; Valiev, R.Z.; Murty, K.L. Influence of grain size on radiation effects in a low carbon steel. *J. Nucl. Mater.* **2013**, *443*, 302–310. [[CrossRef](#)]
20. Sun, C.; Yu, K.Y.; Lee, J.H.; Liu, Y.; Wang, H.; Shao, L.; Maloy, S.A.; Hartwig, K.T.; Zhang, X. Enhanced radiation tolerance of ultrafine grained Fe-Cr-Ni alloy. *J. Nucl. Mater.* **2012**, *420*, 235–240. [[CrossRef](#)]
21. Kurishita, H.; Kobayashi, S.; Nakai, K.; Ogawa, T.; Hasegawa, A.; Abe, K.; Arakawa, H.; Matsuo, S.; Takida, T.; Takebe, K.; *et al.* Development of ultra-fine grained W-(0.25–0.8)wt%TiC and its superior resistance to neutron and 3MeV He-ion irradiations. *J. Nucl. Mater.* **2008**, *377*, 34–40. [[CrossRef](#)]
22. Matsuoka, H.; Yamasaki, T.; Zheng, Y.J.; Mitamura, T.; Terasawa, M.; Fukami, T. Microstructure and mechanical properties of neutron-irradiated ultra-fine-grained SUS316L stainless steels and electrodeposited nanocrystalline Ni and Ni-W alloys. *Mater. Sci. Eng. A* **2007**, *449–451*, 790–793. [[CrossRef](#)]
23. Kaoumi, D.; Motta, A.T.; Birtcher, R.C. Grain growth in nanocrystalline metal thin films under *in situ* ion-beam irradiation. *J. ASTM Int.* **2007**, *4*, 1–13. [[CrossRef](#)]
24. Nita, N.; Schaeublin, R.; Victoria, M.; Valiev, R.Z. Effects of irradiation on the microstructure and mechanical properties of nanostructured materials. *Philos. Mag.* **2005**, *85*, 723–735. [[CrossRef](#)]
25. Borgesen, P.; Lilienflec, D.A.; Msaad, H. Radiation induced grain growth in transition metals. *Mat. Res. Soc. Symp. Proc.* **1991**, *201*, 393–398. [[CrossRef](#)]
26. Karpe, N.; Bottiger, J.; Chechenin, N.G.; Krog, J.P. Ion irradiation induced grain growth in nanocrystalline Fe and Fe (Zr). *Mater. Sci. Eng. A* **1994**, *180*, 582–586. [[CrossRef](#)]
27. Rowcli, A.F. Austenitic stainless steels and high strength copper alloys for fusion components. *J. Nucl. Mater.* **2008**, *263*, 183–192.
28. Zauter, R. Copper in the ITER project. *Adv. Mater. Process.* **2010**, 19–20. Available online: <http://www.asminternational.org/documents/10192/1906196/amp16807p19.pdf/dc3f32c1-f9a9-4269-a006-a87ff657b15e/AMP16807P19> (accessed on 10 January 2015).
29. Björkbacka, Å.; Hosseinpour, S.; Johnson, M.; Leygraf, C.; Jonsson, M. Radiation induced corrosion of copper for spent nuclear fuel storage. *Radiat. Phys. Chem.* **2013**, *92*, 80–86. [[CrossRef](#)]
30. Idaho National Laboratory Advanced Test. *Reactor National Scientific User Facility Users' Guide*; Idaho National Laboratory Advanced Test: Idaho Falls, ID, USA, 2009.
31. Simulia Inc. *ABAQUS 6.11 User's Manual*; Simulia Inc.: Johnston, NC, USA, 2011.
32. Los Alamos National Laboratory. *Volume 1: Overview and Theory X-5 Monte Carlo Team*; Los Alamos National Laboratory: Los Alamos, NM, USA, 2008.
33. Patterson, A.L. The Scherrer formula for X-Ray particle size determination. *Phys. Rev.* **1939**, *56*, 978–982. [[CrossRef](#)]
34. Monshi, A.; Foroughi, M.R.; Monshi, M.R. Modified Scherrer equation to estimate more accurately nano-crystallite size using XRD. *World J. Nanosci. Eng.* **2012**, *2*, 154–160. [[CrossRef](#)]

35. Suryanarayana, C.; Norton, M.G. X-ray diffraction: A practical approach. *Microsc. Microanal.* **1998**, *4*, 513–515.
36. Hansen, N. Hall–Petch relation and boundary strengthening. *Scr. Mater.* **2004**, *51*, 801–806. [[CrossRef](#)]
37. Singh, B.N.; Edwards, D.J.; Toft, P. Effects of neutron irradiation on mechanical properties and microstructures of dispersion and precipitation hardened copper alloys. *J. Nucl. Mater.* **1996**, *238*, 244–259. [[CrossRef](#)]
38. Ghauri, I.M.; Butt, M.Z.; Raza, S.M. Grain growth in copper and alpha-brasses. *J. Mater. Sci.* **1990**, *25*, 4782–4784. [[CrossRef](#)]
39. Murty, K.L.; Charit, I. *An Introduction to Nuclear Materials: Fundamentals and Applications*; WILEY-VCH: Weinheim, Germany, 2013.
40. Was, G.S. *Fundamentals of Radiation Materials Science: Metals and alloys*; Springer: Berlin, Germany, 2007.
41. Sato, A.; Mifune, T.; Meshii, M. Irradiation softening in pure iron single crystals. *Phys. Status Solidi* **1973**, *18*, 699–709. [[CrossRef](#)]
42. Chen, Y. Irradiation effects of Ht-9 martensitic steel. *Nucl. Eng. Technol.* **2013**, *45*, 311–322. [[CrossRef](#)]
43. Ganapathi, S.K.; Owen, D.M.; Chokshi, A.H. The kinetics of grain growth in nanocrystalline copper. *Scr. Metall. Mater.* **1991**, *25*, 2699–2704. [[CrossRef](#)]
44. Neumann, G.; Toelle, V. Monovacancy and divacancy contributions to self-diffusion in face-centered cubic metals: Reanalysis for copper, silver gold nickel and platinum. *Philos. Mag. A* **1986**, *54*, 619–629. [[CrossRef](#)]
45. Li, H.Q.; Ebrahimi, F. An investigation of thermal stability and microhardness of electrodeposited nanocrystalline nickel-21% iron alloys. *Acta Mater.* **2003**, *51*, 3905–3913. [[CrossRef](#)]
46. Michaelsen, C.; Barmak, K.; Weihs, T.P. Investigating the thermodynamics and kinetics of thin film reactions by differential scanning calorimetry. *J. Phys. D Appl. Phys.* **1999**, *30*, 3167–3186. [[CrossRef](#)]
47. Kaoumi, D.; Motta, A.T.; Birtcher, R.C. A thermal spike model of grain growth under irradiation. *J. Appl. Phys.* **2008**, *104*. [[CrossRef](#)]



© 2016 by the authors; licensee MDPI, Basel, Switzerland. This article is an open access article distributed under the terms and conditions of the Creative Commons by Attribution (CC-BY) license (<http://creativecommons.org/licenses/by/4.0/>).